Experimental characterization of SLM and EBM cubic lattice structures for lightweight applications

Experimental characterization of EBM and SLM cubic lattice structures for lightweight applications

G. De Pasquale[1], F. Luceri[1], M. Riccio[2]

[1] Department of Mechanical and Aerospace Engineering, Politecnico di Torino
Corso Duca degli Abruzzi 24, 10129 Torino (Italy)
[2] BeamIt S.p.A., Strada Prinzera 17, 43045 Fornovo di Taro (Italy)
Corresponding author:
E-mail: giorgio.depasquale@polito.it
Phone: +39.011.090.6912
Fax: +39.011.090.6999

Abstract

The experimental characterization of lattice structures based on cubic cells fabricated through selective laser melting (SLM) and electron beam melting (EBM) is presented. The lattice failure under compressive load is studied as a function of the process typology, material properties, and dimensional parameters of the unit cell. The bulk material is preliminarily characterized to evaluate the process stabilization. Three main failure modes of the lattice are identified, depending on the ductile/brittle material response and the direction of crack propagation. The relationship between lattice geometrical parameters and mechanical strength is observed. The equivalent Young's module of lattice samples with different cell size has been measured and compared with numerical simulations based on the homogenization method.

Keywords

Lattice structures; lightweight structures; additive manufacturing; cellular materials; engineered materials; powder melting; lattice failure modes.

1. Introduction

The demand for strong and light structures is motivating researchers in many different academic and industrial fields. The development of advanced components with high strength/mass ratios is under investigation especially in vehicle and transport systems, civil engineering, spatial industry, and aeronautic applications **[1, 2]**. Relevant advancements in the field of lightered structures have been obtained mainly with composite materials and topology optimization methods for metals. Earlier studies in the field of structural optimization have led to the development of several models and algorithms toward modifying the shape of components by decreasing their mass and keeping stresses below certain limits. These calculation strategies, known as topology optimization methods **[3, 4]**, modify the component shape with the use of iterative procedures. Among them are the homogenization method **[5, 6]**, multipoint approximation **[7, 8]**, single-point approximation **[9, 10]**, and combined approximations **[11, 12]**. However, the modern simulation tools for topology optimization do not achieve the best strength/mass ratios; in general, their outputs are geometrically complicated structures with a bulk massive configuration with the same density in the entire volume **[13, 14]**.

To overcome the intrinsic limitations of lightered bulk structures, another design philosophy is needed, which is represented by lattice structures. The design of lattices is pushed to the millimeter (or even submillimeter) scale to define the structural geometry through assembling a few modules with an elementary shape. The lattice design is inspired by natural structures, in which the use of bulk materials is very rare. The resulting structures are also identified as

“biologically inspired” (or bio-inspired) structures due to their similarities with nature. The main advantage of the lattice design is the detailed control and continuous modification of the material equivalent density in every region of the structure. Then, it is possible to control the local strength with high precision and to provide the highest achievable optimization of lightness.

Interest in lattice design is increasing considerably because of the rapid spread of additive manufacturing (AM) technologies, which are suitable for building small and detailed features **[15-21]**. Historically, the applications of AM were limited to the production of prototypes and casting inserts; at present, they include a huge variety of production tools, short-run structural parts, customized bioengineered parts, and mass-customized parts, among others. On the other hand, there is still a lack of knowledge about the linkage between the AM process parameters and the structural performance of products. For this purpose, the World Technology Evaluation Center developed in 2009 the “Roadmap for Additive Manufacturing (RAM): Identifying the Future of Freeform Processing” **[22]**, which includes the following crucial points. Design: a) to create conceptual design methods to aid designers in defining and exploring design spaces enabled by AM; b) to develop computer-aided design systems to overcome the limitations of existing solid modeling in representing complex geometries; c) to provide a multiscale modeling and inverse design methodology to assist in navigating complex process-structure relationships; d) to create methods to model and design with variability: shape, properties, process, etc. Process modeling and control: a) to develop predictive process-structure relationships integrated with CAD/E/M tools; b) to create adaptive control systems with feedforward and feedback capabilities and new sensors. Materials, processes, and

machines: a) to develop a better understanding of the basic physics of AM; b) to create scalable, fast material processing methods; c) to exploit unique AM characteristics to produce epitaxial metallic structures, fabricate functionally gradient materials and multiple materials, and embed components during fabrication processes.

The first models of periodic structures were based on an analogy with cellular materials, such as foams **[23-25]**. Then, several analytic and numerical models were proposed for predicting the behavior of periodic structures **[26, 27]** and lattice structures with various shapes **[28-31]**.

An experimental analysis of the mechanical behavior of lattice structures is needed to validate the predictive models. The limited number of experimental studies in the literature is primarily due to the challenges associated with the fabrication process of lattice samples with the desired accuracy and repeatability. In fact, although powder-based technologies are almost consolidated also for metals, the stabilization of these processes is not easy to obtain. Consistent mechanical characterization activities require repeatable and certifiable processes that can guarantee the same quantifiable output. This requirement involves many issues, including powder control and stabilization, thermal treatment consolidation, machine trials, and post-processing inspection activities. The survey of the literature provides a limited number of relevant contributions to the experimental validation of metal lattices under static loads **[32-37]**, in some cases with focus on strength and strain properties **[38-39]** or even with preliminary fatigue results **[40]**. Lattices made with other materials, such as polymers **[41]**, have also been considered, as well as those with different structure typologies, such as honeycomb **[42]**.

In the present work, samples fabricated by stable, repeatable, and certified SLM and EBM processes are used. The experimental approach applied is inspired by other studies reported in the literature **[43-51]** and consists of the characterization of parameterized samples with a uniform lattice shape and controlled loading conditions. The material (light alloy Ti-6Al-4V) has been preliminarily characterized with the use of tensile tests to investigate the behavior of lattice samples.

There is a linkage between lattice structures (in which each cell is dimensioned by the designer) and traditional cellular materials (in which cells are created randomly and without order), such as foams. In both cases, the structures are formed by repeated modular elements, and the global properties can be related to those of the basic unit cell. The structural collapse of foams is linked to elastic buckling of elastomeric cells (e.g., rubbers), yielding of plastic hinges in cells (e.g., metals), and brittle crushing in brittle cells (e.g., ceramics). Similarly, the energy absorbed by the foam during deformation is linked to the energy absorbed by the cell. The characterization results for lattice structures reported in this work are very similar to the experimental results obtained with cellular materials and foams **[23, 24]**. The failure modes of lattices are also investigated, with particular focus on the direction of fracture propagation; three main failure modes are identified, depending on the material properties, cell geometry, and, indirectly, fabrication process.

2. Equipment

2.1. SLM Processing

The EOS M 290 machine with a 400-W Yb-fiber laser (Tab. 1) is used for the selective laser melting (SLM) process. Several process parameters are modulated with the use of the embedded software, including the laser speed and power, hatch distance and orientation, hatch offset to the part contour (beam offset), and stripe width and offset. SLM is a “cold process” because the powder bed among the parts to be built is not warmed up during the melting. The produced parts present residual stresses; therefore, heat treatments for relieving stress are needed. The volumetric energy density (VED) for SLM process is defined as

$$VED = \frac{P}{vht}$$

where *P* is the laser power, *v* is the laser speed, *h* is the hatching distance and *t* is the layer thickness. The SLM process setup used in this work has VED = 37.78 J/mm^3.

2.2. EBM Processing

The Arcam Q10 machine (Tab. 1) is used for the electron beam melting (EBM) process. This system is particularly suitable for building biomedical components because the vacuum chamber is designed to contain the most common implants. The electron beam gun can achieve a laser beam power of 3000 W and a high scan speed of 8000 m/s. Different process parameters can be set to produce either bulk or thin structures, with good results. In contrast to SLM, EBM is a “hot process” because each layer is warmed up to 750 °C by scanning the powder bed with an electron beam. Thus, no heat treatments for relieving stress are needed.

The VED for EBM process is defined accordingly to [XXX] as

$$VED = \frac{UI_b}{vht}$$

where U is the acceleration voltage, I_b is the beam current, v is the scan speed, h is the hatching distance, and t is the layer thickness. The EBM process setup used in this work has VED = 19.86 J/mm^3.

Tab. 1. Technical data of SLM (EOS M290) and EBM (Archam Q10) machines.

Property	*SLM*
Building volume	250x250x325 mm
Laser type	Yb-fibre laser, 400 W
Max scan speed	7.0 m/s
Max beam power	400 W
Focus diameter	100 µm
Compressed air supply	7000 hPa, 20 m^3/m
Property	*EBM*
Building volume	200x200x180 mm
Cathode type	single crystalline
Max scan speed	8000 m/s
Max beam power	3000 W
Vacuum base pressure	$1 \cdot 10^{-5}$ mbar

2.3. Other instrumentation

After fabrication process, SLM samples are subjected to heat treatments for stress relief. A customized TAV vacuum furnace (300x240x150-mm capacity, 1400°C maximum temperature) is used for this purpose. The furnace can force gas convection during thermal cycles to improve the temperature uniformity and heating speed in the internal regions of massive components. Gas quenching is applied to ensure metallurgical and mechanical transformation without excessive distortion.

The Sonica 3300 EP ultrasonic cleaner (9.5-l tank capacity, 300-W power heating, 70°C maximum operating temperature) is then used to remove contaminants from SLM and EBM samples. The ultrasonic cleaning mechanism includes an electronic generator coupled with

piezoelectric transducers that can mechanically excite the cleaning fluid. The vibrating signal causes pressure waves in the fluid at about 40 kHz and the formation of micro-bubbles, which impact against the solid surfaces of the samples and achieve mechanical cleaning.

In the next step, SLM and EBM samples are separated into two sections to allow internal inspection and to analyze the properties and topology of lattices. The ATM Brillant 250 wet abrasive cut-off machine is used to cut the samples. This machine has a cutting wheel 356mm in diameter and provides coolant recirculation for heating prevention and debris removal. The Zeiss Axio Observer optical microscope with 350nm vertical resolution is used for morphological detection. After cutting, each sample is encapsulated in resin and subjected to one hour of heating. Then, the encapsulated samples are polished with sandpaper and analyzed under the optical microscope to evaluate the internal topology.

After optical inspection of some sacrificial samples, other SLM and EBM bulk and lattice samples are characterized mechanically. The Instron 8801 servohydraulic testing machine with 100-kN maximum load capacity is used at this purpose. This machine can perform static and dynamic tests (low/high cycle fatigue), thermomechanical fatigue testing, and fracture mechanics. The system is equipped with digital controller and dynamic load cell.

3. Samples for material characterization

The first sample typology addresses the characterization of material properties after SLM and EBM processes. The light alloy Ti-6Al-4V is chosen because it is largely used for building biomedical components and is suitable for post-process heat treatments and lattice structure

fabrication **[52, 53]**. The powder granulometry has a Gaussian distribution range of 15-45 μm for SLM and 45-106 μm for EBM.

The bulk samples used for the material stress-strain curve evaluation under tensile test have central region with uniform stress (40mm long and 5mm wide) and two clamping borders (12mm long and 8mm wide); the thickness is 0.6mm. The shape and dimensions are shown in Fig. 1 and Tab. 2. The nominal thickness of the samples corresponds to the average strut thickness in lattice structures, to reproduce the same failure mechanisms. Two sample sets are fabricated by using SLM and EBM processes, respectively. For each set, two growth orientations (horizontal and vertical) are considered to evaluate possible variations in mechanical strength in the lattice struts. Five sample replications per combination set (total of 20 samples) are fabricated and tested to provide statistical confidence to the results.

The tests are conducted at ambient temperature and 0.4 mm/min velocity in displacement control mode. The load is applied until the rupture. The application of strain gauges is impeded by the small size and low stiffness of samples. However the measurement of displacement, which has the resolution of 10^{-3}mm, is not affected by significant errors because the mechanical parts of the machine are loaded at only 2.4% of the load capacity due to sample characteristics. The load cell accuracy in detecting the applied force is +/- 0.5%.

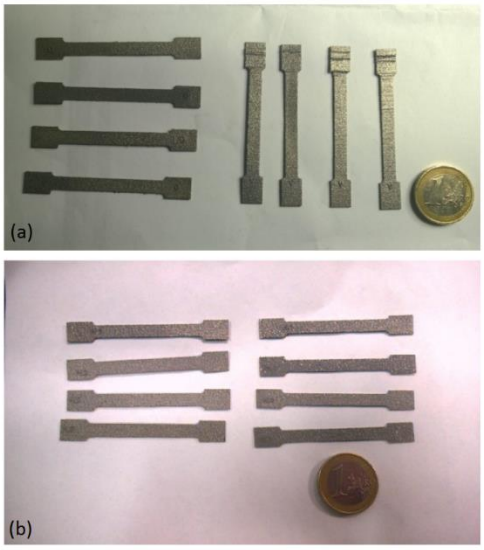

Fig. 1. Samples for Ti-6Al-4V mechanical characterization fabricated with SLM (a) and EBM (b) processes.

Tab. 2. Nominal and measured dimensions of samples for material characterization fabricated with SLM and EBM processes.

	Nominal dimension	*Measured dimension*	*Standard deviation*
SLM samples			
Length	40.00 mm	41.15 mm	0.350 mm
Thickness	0.60 mm	0.74 mm	0.025 mm
Width	5.00 mm	5.09 mm	0.079 mm
Area	3.00 mm^2	3.76 mm^2	-
EBM samples			
Length	40.00 mm	41.15 mm	0.239 mm
Thickness	0.60 mm	0.81 mm	0.025 mm
Width	5.00 mm	5.14 mm	0.100 mm
Area	3.00 mm^2	4.18 mm^2	-

4. Lattice samples

The lattice samples are designed according to the following variants: cell dimensions, strut thickness, and cell staggering (symmetric or asymmetric). The number of cells is varied among samples to obtain approximately the same size of all lattices. The parametric dimensions are used to evaluate the effect of the cell and strut sizes on the structural properties. The dimensions are selected by considering the limits imposed by each process, especially on the

length of suspended parts. In general, the EBM process uses preheated powder with increased compactness, which allows longer struts compared with the SLM process. The samples are organized on the machine stage to optimize the number of fabrication jobs, as shown in Fig. 2a for the EBM process. After the powder melting process, the SLM samples are subjected to heat treatment for stress relief and mechanical strength stabilization, after which they are removed from the metal stage by using an electro-discharge machine and then sandblasted. In contrast, the EBM samples are sandblasted just after the fabrication process. All samples are washed with an ultrasonic cleaner and then dried to remove any residual powder from inside the cavities.

Preliminary EBM and SLM process calibration based on the design of experiments (DOE) is carried out to define the best process parameters for fabricating lattice samples. The final dimensions of the lattice samples are shown in Tab. 3, with reference to Fig. 2b, where t is the strut thickness, l is the cell size, B is the sample width/length, and H is the sample height. Figure 2c and d shows the final lattice samples after the SLM and EBM additive processes.

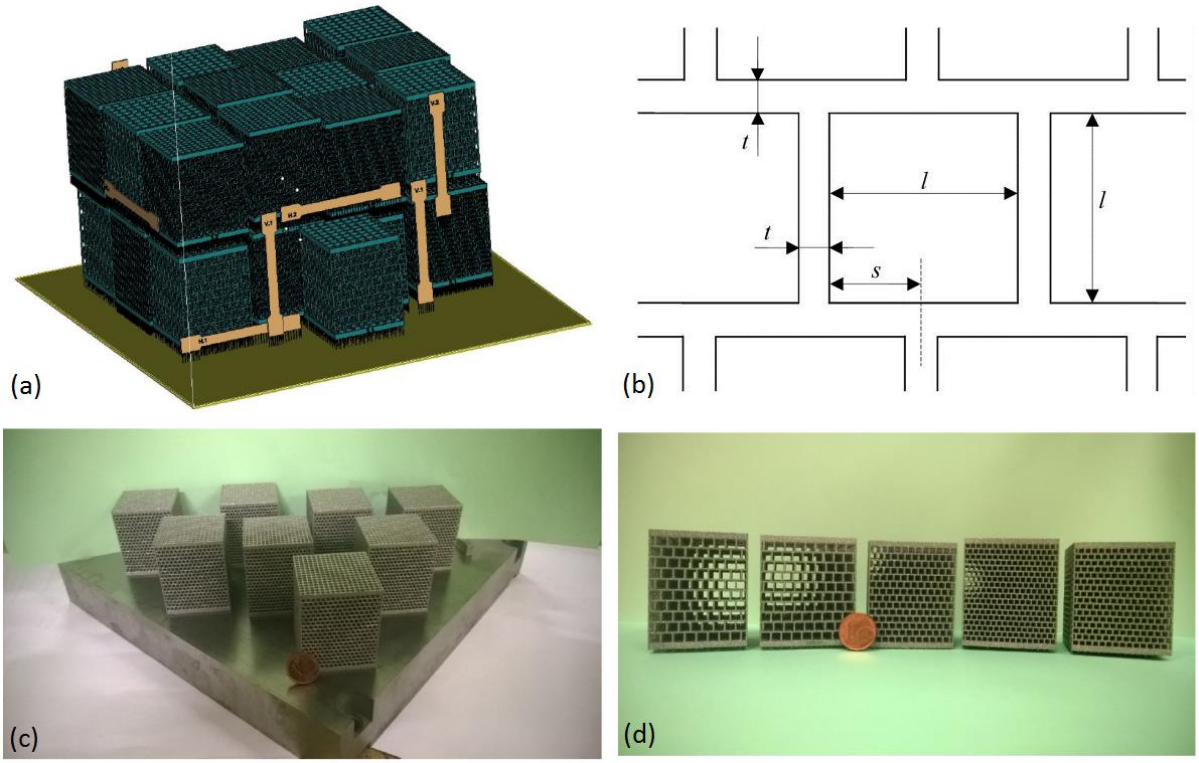

Fig. 2. Organization of samples in the operational volume of EBM machine (a), lattice geometrical parameters (b), lattice samples fabricated with SLM (a) and EBM (b) additive processes.

Tab. 3. Lattice samples dimensions.

Sample	*t [mm]*	*l [mm]*	*Number of cells*	*s*	*Volume BxBxH [mm³]*
			SLM samples		
1-SLM	0.40	1.50	20x20x23	$l/2$	38.78x38.78x48.54
2-SLM	0.50	1.65	17x17x20	$l/2$	38.34x38.34x47.70
3-SLM	0.60	1.70	16x16x19	$l/2$	38.22x38.22x47.88
			EBM samples		
1-EBM	0.64	3.60	8x8x10	$l/2$	36.30x36.30x46.60
2-EBM	0.60	3.60	9x9x10	$l/4$	39.45x39.45x46.60
3-EBM	0.40	2.60	12x12x14	$l/2$	37.90x37.90x46.40
4-EBM	0.40	2.00	16x16x18	$l/2$	40.00x40.00x47.60
5-EBM	0.60	2.00	14x14x16	$l/2$	38.30x38.30x46.20

5. Results of material characterization

The samples for material characterization described in Section 3 are subjected to tensile tests with the use of the Instron 8801 hydraulic machine. Figure 3 shows the stress-strain curves of the SLM and EBM samples, respectively, considering the difference between the horizontal and the vertical orientation during the additive process. Tab. 4 presents the measured Young's moduli for all samples. Figure 4 shows the fracture surfaces of some significant SLM and EBM samples.

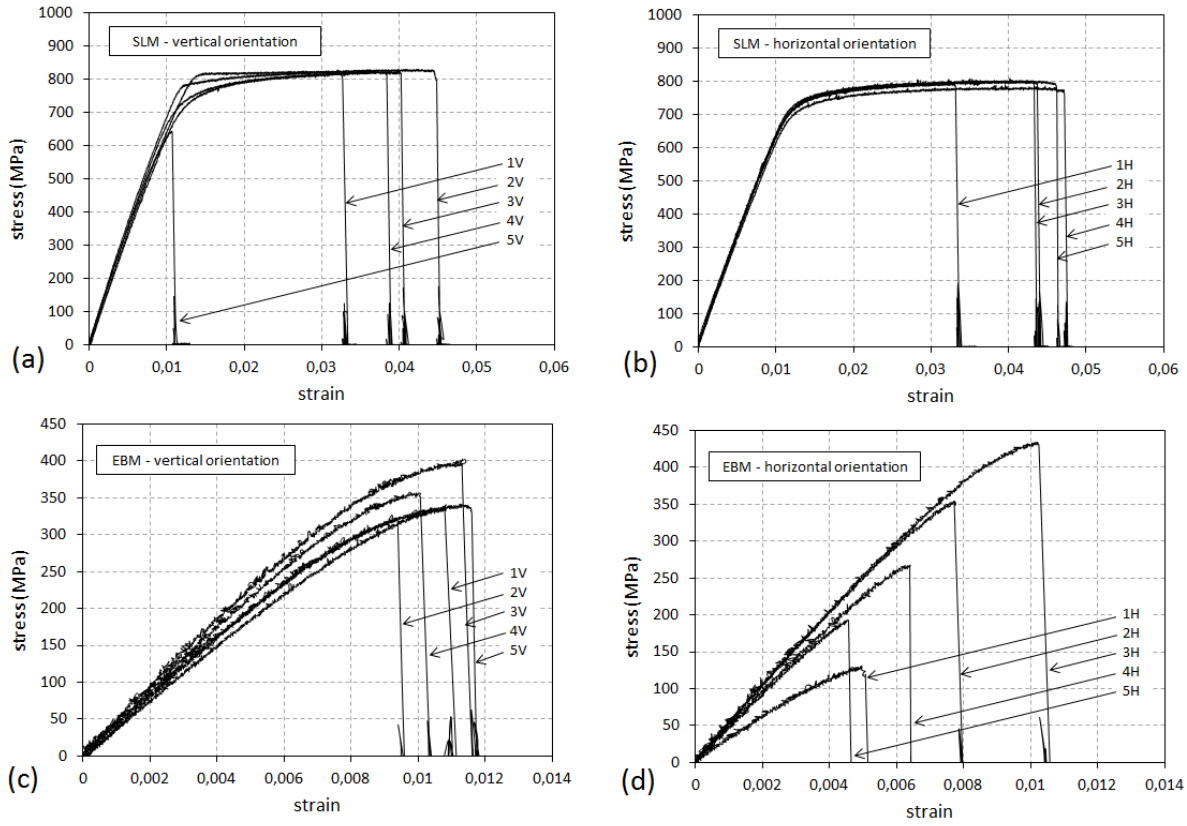

Fig. 3. Stress-strain curve of Ti-6Al-4V samples fabricated with SLM in vertical (a) and horizontal (b) growth orientations and with EBM in vertical (c) and horizontal (d) growth orientations.

Tab. 4. Young's modulus of SLM and EBM samples as function of orientation.

		Young's modulus [MPa]		
Sample	*Orientation*	*Measured value*	*Average*	*Std. dev*

SLM Samples				
1V		64.726		
2V		65.267		
3V	Vertical	67.731	64.390	2.530
4V		63.329		
5V		60.864		
1H		69.884		
2H		62.930		
3H	Horizontal	60.711	63.411	3.792
4H		60.607		
5H		62.923		
EBM Samples				
1V		36.721		
2V		34.869		
3V	Vertical	38.171	36.431	2.811
4V		39.800		
5V		32.596		
1H		22.486		
2H		42.273		
3H	Horizontal	45.865	38.349	9.164
4H		41.569		
5H		39.778		

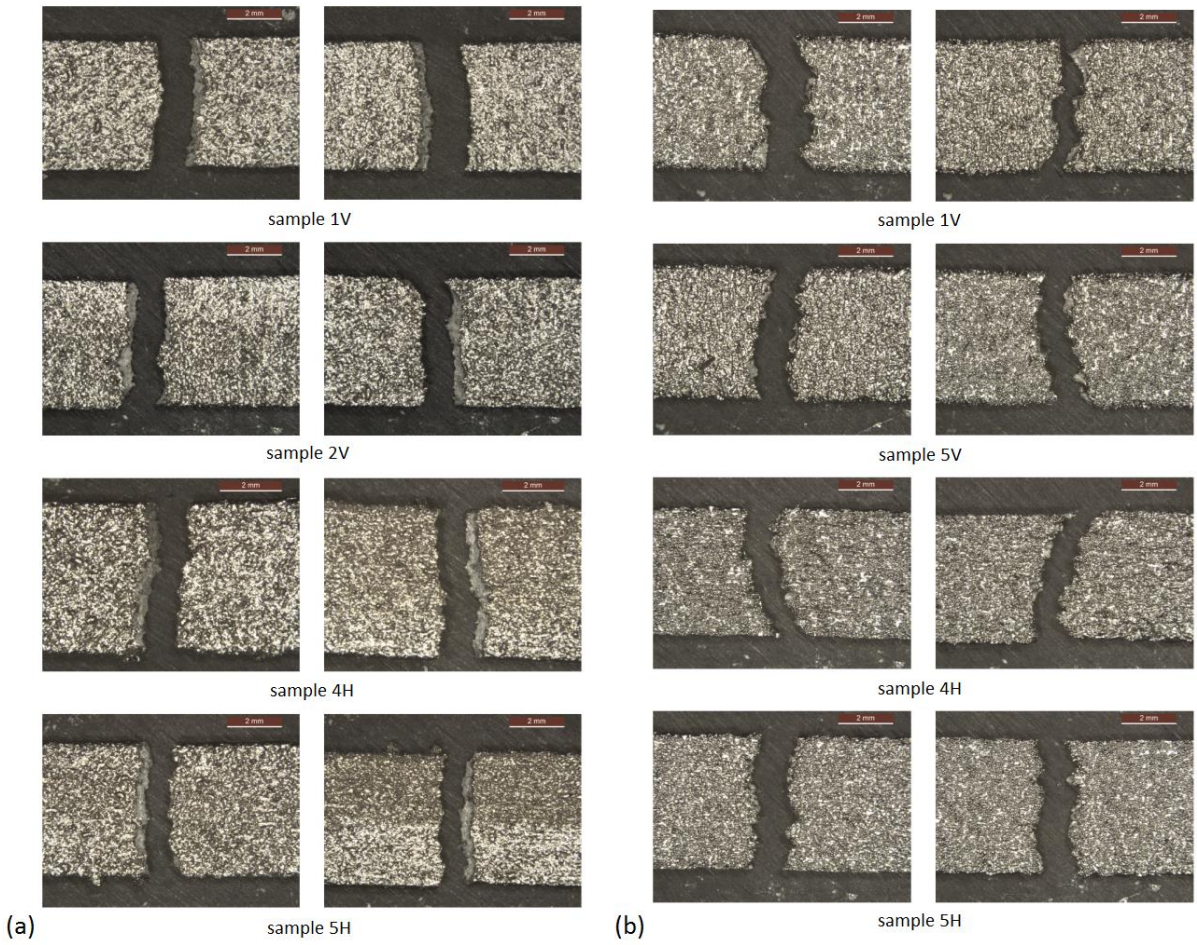

Fig. 4. Fracture surfaces of some significant SLM (a) and EBM (b) samples; both sides of the sample are reported.

6. Results of lattice compression tests

The compression tests are carried out in position control mode at 25 mm/min velocity and ambient temperature. Two samples per typology are tested.

6.1. SLM lattice

Figure 5 shows the load-displacement curve for the SLM samples. Each peak corresponds to the collapse of one lattice layer. After every collapse, the load decreases because of the reduced

strength of the damaged layer. Also, the compressive plates of the machine experiences small oscillations, which are visible in the diagrams before the beginning of each load step. At the end of the compression curve, the load increases monotonically due to the complete densification of the lattice. Sample 3-SLM shows high mechanical strength, exceeding the maximum compressive force applicable by the machine (100 kN).

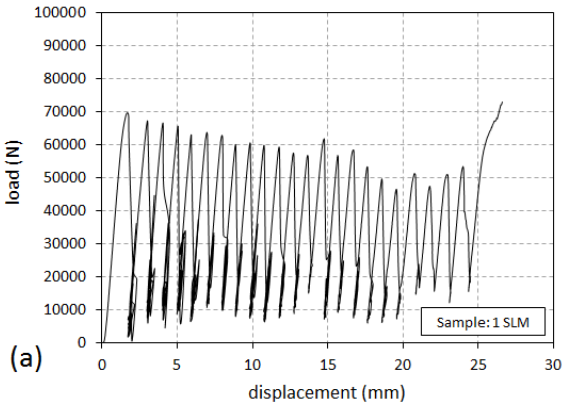

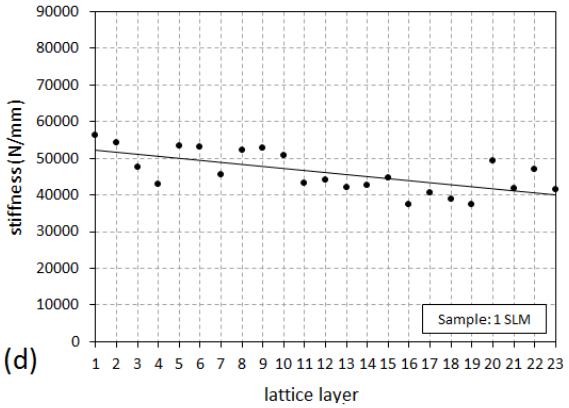

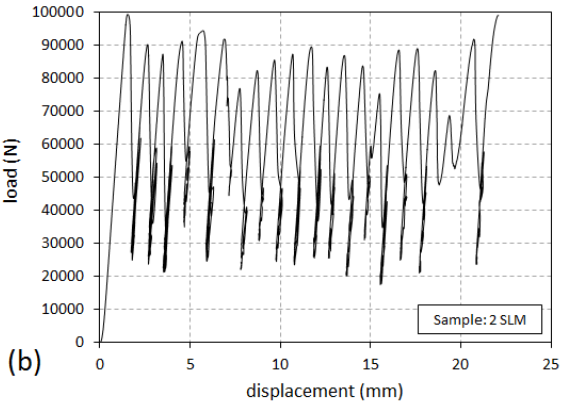

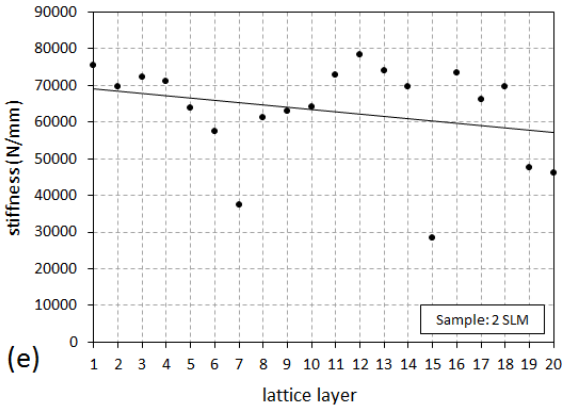

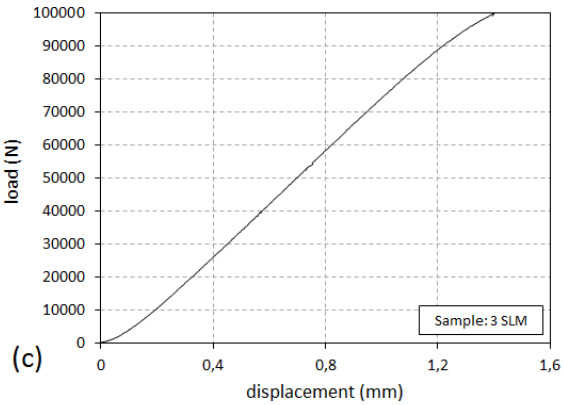

Fig. 5. Experimental load-displacement curves of SLM lattice samples (a, b, c) and variation of lattice stiffness during layers collapse for samples 1-SLM (d) and 2-SLM (e).

The slope of each peak is used to determine the stiffness variation of the lattice samples during the successive layer collapse. Finally, the trends reported in Fig. 5d and e are obtained for samples 1-SLM and 2-SLM. The initial compressive stiffness of the lattice sample (before the first cell collapse) is particularly relevant to validate the numerical and analytical models of elastic response of lattice structures. Table 5 shows the first peak stiffness measured on six SLM samples (two samples per typology). Figure 7a presents the sequence of collapse of sample 1-SLM.

Tab. 5. Experimental compressive stiffness of SLM lattice samples before first cell collapse.

	k_{exp} [N/mm]		
Sample	Test 1	Test 2	Error [%]
1-SLM	56157	56077	-0,14
2-SLM	73885	75516	2,21
3-SLM	76433	79262	3,70

6.2. EBM lattice

Figure 6a to f shows the load-displacement curve of the EBM samples. Differently from the SLM samples, single cells fail simultaneously in different positions. The failure modes are described in greater detail in Section 8. Figure 6f to j presents the trend in stiffness variation obtained from the slope of each force-displacement peak. Table 6 shows the first peak stiffness measured on the five EBM samples. The sequence of collapse of sample 2-EBM is presented in Fig. 7b.

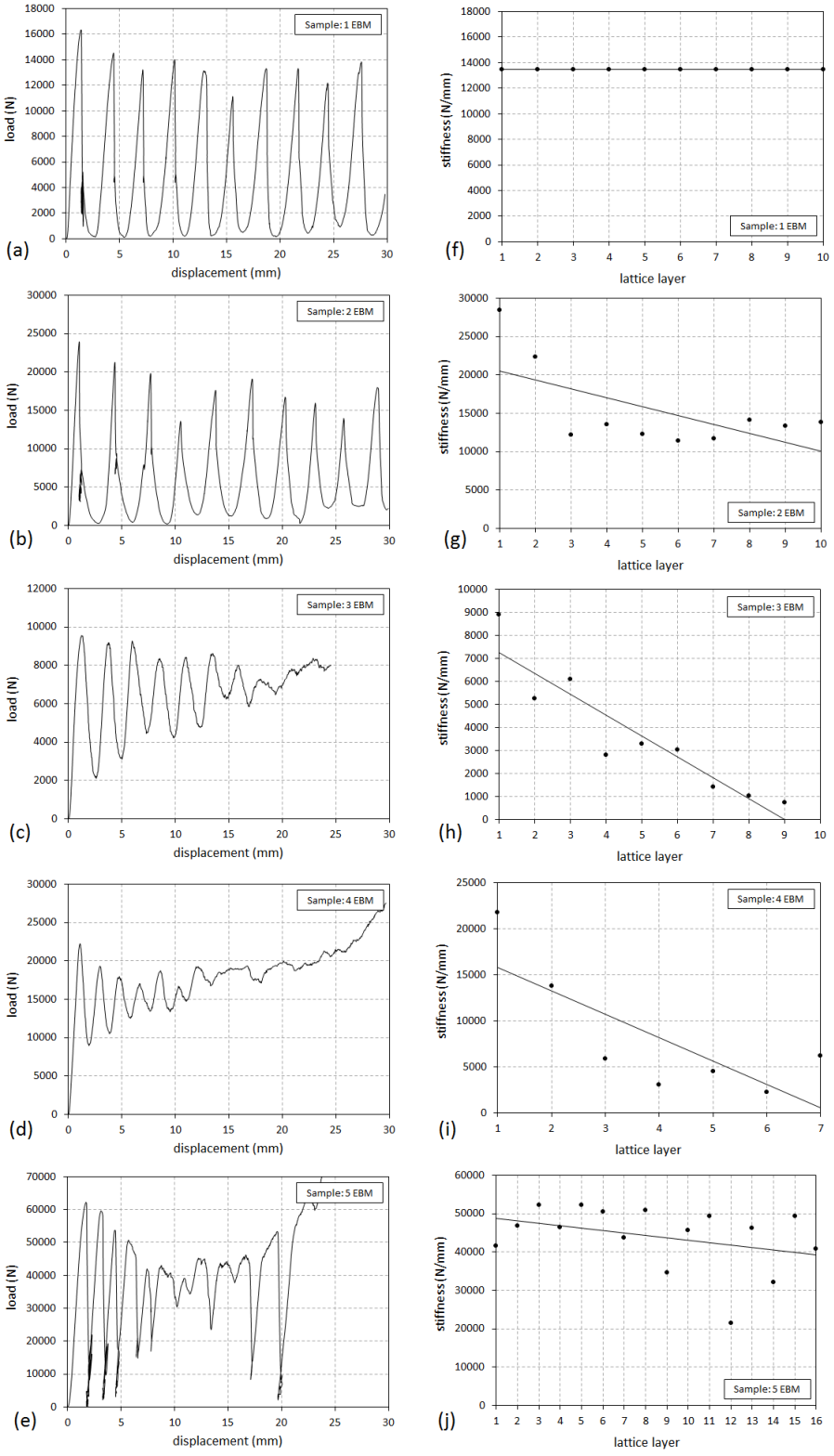

Fig. 6. Experimental load-displacement curves of EBM lattice samples (a-e) and variation of lattice stiffness during layers collapse (f-j).

Tab. 6. Experimental compressive stiffness of EBM lattice samples.

	k_{exp} [N/mm]		
Sample	Test 1	Test 2	Error [%]
1-EBM	13649	13455	-1,42
2-EBM	28424	29111	2,42
3-EBM	8889	9090	2,26
4-EBM	21618	21777	0,74
5-EBM	54911	52210	-4,92

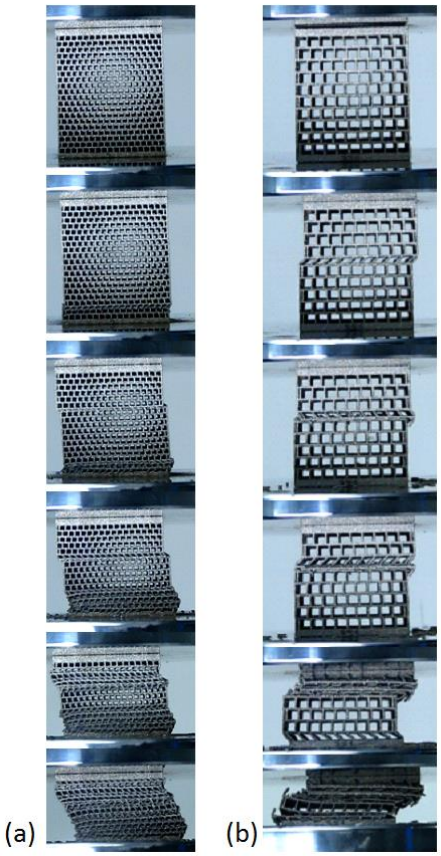

Fig. 7. Collapse sequence of samples 1-SLM (a) and 2-EBM (b).

7. Numerical modeling

The homogenization method is used to develop a numerical model capable of predicting the equivalent structural properties of lattice materials. Cellular structures can be compared with composite materials consisting of bulk Ti-6Al-4V alloy and vacuum as constitutive phases. Then,

the representative volume element (RVE) can be modeled as an equivalent homogeneous anisotropic continuum **[54-56]**. The detailed study of local properties (e.g., stress and strain) requires investigation at the lattice scale; however, these properties are not relevant to the evaluation of the structural behavior of the whole lattice material and thus are not considered in the present analysis. In other words, the homogenization method allows replacing at the macroscopic scale the true (and complex) geometry of the RVE with an equivalent homogeneous medium whose mechanical response is described by a set of "effective" (or equivalent) material properties. These properties can be computed through different homogenization schemes, such as the volume average stress–based method and the strain energy method. Furthermore, although the bulk material constituting the lattice is isotropic, its macroscopic behavior (i.e., after homogenization) is generally anisotropic due to the shape and geometry of the RVE.

Through the homogenization method, the equivalence between the strain energy of the RVE and that of the equivalent homogeneous material is imposed. This assumption allows defining the stiffness matrix [K] of the equivalent homogeneous material. Then, the periodic distribution of cells can be used to set boundary conditions for the single RVE. These constraints are applied to the RVE to obtain non-zero components of the strain field in only one direction, as described below.

The constitutive law for the equivalent homogeneous material is

$$\{\bar{\sigma}\} = [K]\{\bar{\varepsilon}\} \tag{1}$$

where $\{\bar{\sigma}\}$ and $\{\bar{\varepsilon}\}$ are the stresses and strains of the equivalent homogeneous continuum, respectively. The stiffness matrix components are calculated, column by column, by solving six

linear static analyses. In each static analysis, the boundary conditions are imposed to provide only one non-zero component of the RVE average strain field. The non-zero strain field component is arbitrarily imposed as equal to the unit; then, the stiffness matrix components [*K*] are estimated as

$$K_{\alpha i} = \bar{\sigma}_{\alpha} = \frac{1}{V}\int_V \sigma_{\alpha i}(x_1, x_2, x_3)dV \tag{2}$$

where *V* is the volume; and $\alpha = 1,...,6$ and $i = 1,...,6$ correspond to the actual static case. Finally, the Young's moduli of the homogenized material can be calculated from the compliance matrix $[B] = [K]^{-1}$ as

$$E_1 = \frac{1}{B_{11}};\quad E_2 = \frac{1}{B_{22}};\quad E_3 = \frac{1}{B_{33}} \tag{3}$$

The RVE is identified inside the lattice samples, as shown in Fig. 8a, except for sample 2-EBM, which has asymmetric beam staggering ($s = l/4$) and thus is not considered. The RVE is modeled with 3D 20-node solid elements (Fig. 8b) to carry out the six static linear analyses after imposing boundary conditions. The homogenization method is used to predict the Young's moduli measured by experiments along the loading direction. The numerical value of the Young's moduli considered is E_1, as expressed by Eq. (3). The experimental value can be expressed as

$$E_{\text{exp}} = k_{\text{exp}}\frac{H}{B^2} \tag{4}$$

where k_{exp} is the experimental stiffness. Table 7 shows the results of the numerical homogenized and experimental values of the Young's moduli.

Tab. 7. Comparison between numerical homogenized and experimental Young's moduli.

Sample	Young's module [MPa]			Errors [%]	
	Experimental (E_{exp})		Homogenized		
	Test 1	Test 2	(E_1)	Test 1	Test 2
1-SLM	1812.5	1810.0	1865.0	2.89	3.04
2-SLM	2397.6	2450.5	2674.8	11.5	9.15
3-SLM	2505.3	2598.0	3070.2	22.5	18.2
1-EBM	482.7	475.8	403.5	-16.4	-15.2
3-EBM	287.1	293.6	259.3	-9.70	-11.7
4-EBM	643.1	647.9	584.6	-9.10	-9.77
5-EBM	1729.4	1644.4	1550.2	-10.4	-5.73

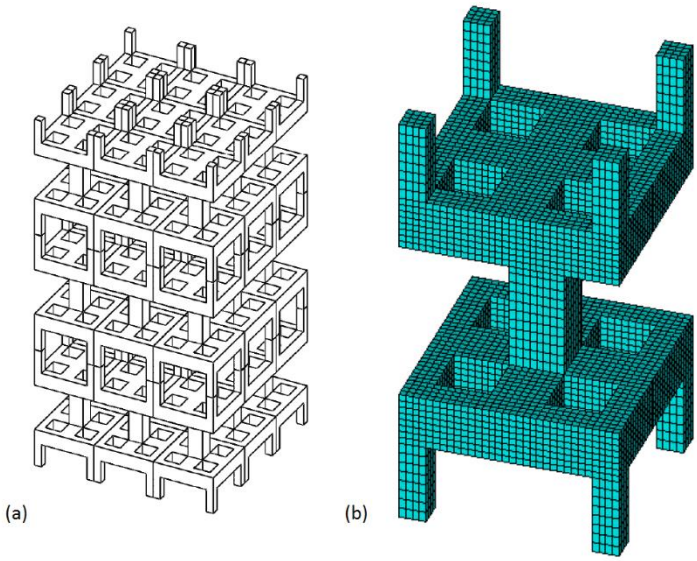

Fig. 8. Representative volume element (RVE): lattice sample composition (a) and finite elements discretization for homogenization method (b).

8. Discussion

8.1. Material characterization

Tensile tests were carried out on 10 SLM samples (5 horizontal and 5 vertical) at 0.4 mm/min in position control. The SLM samples experienced ductile fracture, as demonstrated by the stress-stain diagrams of Figs. 3a-3b where yielding point is visible. The indirect confirmation of this

behavior is provided by the micrographs in Fig. 4a, which shows the fracture surfaces oriented about 45° relative to the loading axis. Additionally, the stress-strain curve shows a large plastic deformation region before the fracture (Fig. 3a and b).

Tensile tests were done on 10 EBM samples (5 horizontal and 5 vertical) at 0.4 mm/min in position control. The EBM samples experienced brittle fracture, as demonstrated by the stress-stain diagrams of Figs. 3c-3d, which does not show plastic deformation. The indirect confirmation of this behavior is provided by the micrographs in Fig. 4b, which shows the fracture surfaces oriented about 90° relative to the loading axis.

The SLM samples showed comparable ultimate stress and strain values for the vertical and horizontal orientations. In the EBM samples, the horizontal orientation caused a slightly higher dispersion of ultimate stress and strain values. The Young's moduli are very similar for the two orientations for the SLM and EBM samples, as shown in Tab. 5.

The higher dispersion of EBM experimental curves can be explained by the lower dimensional accuracy of the EBM process compared with SLM. Additionally, the brittle fracture is initiated by local defects that are very sensitive to single sample features. The plastic deformation of the SLM samples instead involves energy dissipation over a larger area, which is less sensitive to local material defects.

8.2. Lattice structure characterization

Three main modes of lattice collapse under compressive load have been observed, as shown in the schematic drawing in Fig. 9a.

Mode 1 is associated with buckling of the strut intersections (buckling of hinges) and involves one entire layer of the sample at the same time; the compressive load induces structural instability in the direction orthogonal to the load and causes instability of vertical struts at the hinges.

Mode 2 is related to the brittle fracture of horizontal struts primarily due to shear forces; the collapse involves a single or a few lattice cells with unpredictable locations in the lattice and is induced by a local critical combination of ultimate stress and material singularities/defects, which initiates the brittle fracture.

Mode 3 is a combination of first and second modes.

The first failure mode has been observed on both SLM (ductile) and EBM (brittle) lattice samples, whereas the second and third failure modes have been observed only on EBM brittle samples, as presented in Fig. 9 to e for several samples.

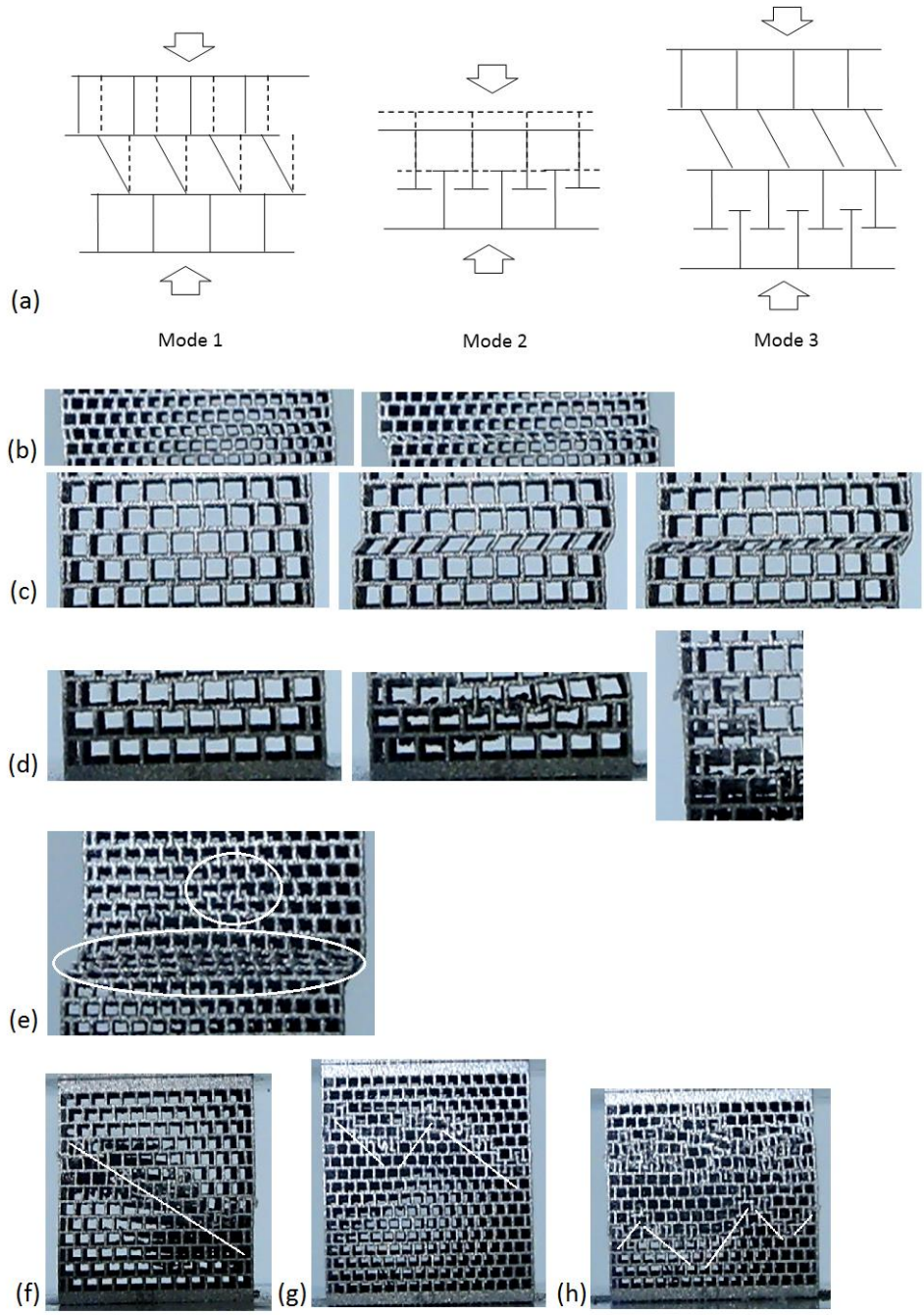

Fig. 9. Failure modes of cubic lattice structures (a). Mode 1 due to hinges buckling: sample 2-SLM (b) and sample 2-EBM (c), mode 2 due to brittle fracture of horizontal struts: sample 1-EBM (d), mode 3 due to mixed failures: sample 6-EBM (e). Directions of densification (sample 3-EBM) of about 45°, lattice collapse due to brittle shear fracture of horizontal struts (f). Directions of lattice fracture (sample 5-EBM) at 45° (g, h).

Failure mode 1 causes lattice densification in the direction orthogonal to the load (namely, at 90° orientation) because the entire layer is involved in the collapse.

In Mode 2 (brittle fracture of horizontal struts), the cubic lattice cell shape causes local densification regions with 45° orientation, as shown in Fig. 9 to h (samples 3-EBM and 5-EBM). This effect, which is associated with the geometry of the lattice cell, can be used to control the directions of lattice collapse and energy absorption in applications in which these parameters are crucial (e.g., impact absorbers).

In conclusion, the behavior of cubic lattice structures as a function of the material properties, fabrication process, and lattice dimensional parameters is investigated. The failure modes of lattices under compressive load are divided into three groups. The results indicate the high potential of lattices, especially from the SLM process, in satisfying the requirements of high strength and lightness in many applications at present and in the immediate future.

8.3. Numerical modeling

The numerical modeling through the homogenization method shows good prediction of the real Young's moduli, with error rates of between 2% and 22%. The higher accuracy is obtained from simulating lattice samples with the highest number of cells: in this case, border effects are less relevant, and the lattice structure is closer to the homogeneous condition than in the case of large cells. The errors associated with border effects include two sources of inaccuracy: first, the cells situated at the periphery of the sample have a different constraining condition from

those situated internally; and second, the shape of the RVE is slightly different for cells at the sample periphery.

9. Conclusions

The mechanical properties of lattice samples are evaluated and compared with the predictions of a numerical model based on the homogenization method. The results of this experimental study show a strong connection between the AM process parameters, materials, and final properties of the lattice. The parametric approach used to design the samples provides detailed results for validating numerical and analytic models of the static strength of lattices. The failure modes of the lattice samples are grouped into three typologies, depending on the material properties and cell orientation. The lattice failure modes in the plastic field under compressive loads indicate the presence of preferential directions of energy dissipation; this property has high potential usefulness in designing components for impact absorption with decreased volume and mass.

References

[1] Brennan-Craddock J, Brackett D, Wildman R, Hague R (2012). The design of impact absorbing structures for additive manufacture. J Phys Conf Ser 382, 012042

[2] Eshraghi S, Das S (2012). Micromechanical finite-element modeling and experimental characterization of the compressive mechanical properties of polycaprolactone-hydroxyapatite composite scaffold prepared by selective laser sintering for bone tissue engineering. Acta Biomater 8, 3138-3143

[3] Prager W (1974). Introduction to structural optimization, Springer Verlag, Vienna.

[4] Rozvany GI (1997). Aims, scope, basic concept and methods of topology optimization, in: Topology optimization in structural mechanics, Springer.

[5] Bakhvalov N, Panasenko G (1989). Homogenization: averaging process in periodic media, Kluwer, Dordrecht.

[6] Bendsøe MP, Kikuchi N (1988). Generating optimal topologies in structural design using a homogenization method. Comp Meth Appl Mech Eng 71, 197-224.
[7] Noor AK (1994). Recent advances and applications of reduction methods. Appl Mech Rev 47, 125-146.
[8] Kirsch U (1993). Structural optimizations, fundamentals and applications. Springer-Verlag, Heidelberg.
[9] Fuchs MB (1980). Linearized homogeneous constraints in structural design. Int J Mech Scie 22, 333-400.
[10] Schmit LA, Farshi B (1974). Some approximation concepts for structural synthesis. AIAA J 11, 489-494.
[11] Kirsch U (1991). Reduced based approximations of structural displacements for optimal design. AIAA J 29, 1751-1758.
[12] Kirsch U, Toledano G (1983). Approximate reanalysis for modifications of structural geometry" Computers and Structures 16, 269-279.
[13] Choi W, Kim J, Park G (2016). Comparison study of some commercial structural optimization software systems. Struct Multidisc Optim 54, 685-699.
[14] Booth W, Alperovich J, Chawls P, Ma J, Reid TN, Ramani K (2017). The design for additive manufacturing worksheet. J Mech Des 139, 100904.
[15] Fraizer WE (2014). Metal additive manufacturing: a review. J Mater Eng Perform 23, 1917-1928.
[16] Gibson I, Rosen D, Stucker B (2015). Additive manufacturing technologies, Second Edition, Springer.
[17] Chu J, Engelbrecht S, Graf G, Rosen DW (2010). A comparison of synthesis methods for cellular structures with application to additive manufacturing. Rapid Prototyping J 16, 275-283.
[18] Ahmadi SM, Yavari SA, Wauthle R, Pouran B, Schrooten J, Weinans H, Zadpoor AA (2015). Additively manufactured open-cell porous biomaterials made from six different space-filling unit cells: the mechanical and morphological properties. Materials 8, 1871-1896.
[19] Scipioni Bertoli U, Wolfer AJ, Matthews MJ, Delplanque JP, Schoenung JM (2017). On the limitations of volumetric energy density as a design parameter for selective laser melting. Materials and Design 113, 331-340.
[20] Rashed MG, Ashraf M, Mines RA, Hazell PJ (2016). Metallic microlattice materials: a current state of the art on manufacturing, mechanical properties and applications. Mater Design 95, 518-533.
[21] Quadbeck P, Kummel K, Hauser R, Standke G, Adler J, Stephani G (2010). Open cell metal foams - Application-oriented structure and material selection. Proc. of CellMat 2010, Dresden, Germany, 279-288.
[22] Bourell DL, Leu MC, Rosen DW (2009). Roadmap for Additive Manufacturing: Identifying the Future of Freeform Processing, Univ. of Texas.
[23] Gibson LJ, Ashby MF (1981). The mechanics of three-dimensional cellular materials, Royal Society Publishing.
[24] Gibson LJ, Ashby MF (1999). Cellular solids: structure and properties. Cambridge University Press.
[25] Ashby MF, Medalist RM (1983). The mechanical properties of cellular solids. Metall Trans A 14, 1755–1769.
[26] Ju J, Summers JD (2011). Compliant hexagonal periodic lattice structures having both high shear strength and high shear strain. Mater Design 32, 512-524.

[27] Coulais C (2016). Periodic cellular materials with nonlinear elastic homogenized stress-strain response at small strains. Int J Solids Struct 97-98, 226-238.
[28] Deshpande VS, Fleck NA, Ashby MF (2001). Effective properties of the octet-truss lattice material. J Mech Phys Solids 49, 1747-1769.
[29] Ushijima K, Cantwell WJ, Chen DH (2013). Prediction of the mechanical properties of micro-lattice structures subjected to multi-axial loading. Int J Mech Sci 68, 47-55.
[30] Smith M, Guan Z, Cantwell WJ (2013). Finite element modeling of the compressive response of lattice structures manufactured using the selective laser melting technique. Int J Mech Sci 67, 28-41.
[31] Dong G, Tang Y, Zhao YF (2017). A survey of modeling of lattice structures fabricated by additive manufacturing. J Mech Des 139, 100906.
[32] Wallach JC, Gibson LJ (2001). Mechanical behavior of a three-dimensional truss material. Int J Solids Struct 38, 7181-7196.
[33] Hao L, Raymont D, Yan C, Hussein A, Philippe Y (2011). Design and additive manufacturing of cellular lattice structures. Proc. VRAP 2011, Leiria, Portugal. doi: 10.1201/b11341-40
[34] Park SI, Rosen DW, Choi SK, Duty CE (2014). Effective mechanical properties of lattice material fabricated by material extrusion additive manufacturing. Additive Manufacturing 1-4, 12-23.
[35] Niu J, Choo HL, Sun W, Mok SH (2017). Numerical study on load-bearing capabilities of beam-like lattice structures with three different unit cells. Int J Mater Des
[36] Banhart J (2001). Manufacture, characterization and application of cellular metals and metal foams. Prog Mater Sci 46, 559-632.
[37] Malek S, Gibson L (2015). Effective elastic properties of periodic hexagonal honeycombs. Mech Mater 91, 226-240.
[38] Blazy JS, Marie-Louise A, Forest S, Chastel Y, Pineau A, Awade A, Grolleron C, Moussy, F (2004). Deformation and fracture of aluminium foams under proportional and non proportional multi-axial loading: statistical analysis and size effect. Int J Mech Sci 46, 217-244.
[39] Mahshid R, Hansen HN, Højbjerre K L (2016). Strength analysis and modeling of cellular lattice structures manufactured using selective laser melting for tooling applications. Mater Design 104, 276-283.
[40] Brandl E, Heckenberger U, Holzing V, Buchbinder D (2012). Additive manufactured AlSi10Mg samples using selective laser melting (SLM): microstructure, high cycle fatigue, and fracture behavior. Mater Design 34, 159-169.
[41] Niu J, Choo HL, Sun W (2016). Finite element analysis and experimental study of plastic lattice structures manufactured by selective laser sintering. Proc. IMechE Part L 231, 171-178.
[42] Jin T, Zhou Z, Wang Z, Wu G, Shu X (2015). Experimental study on the effects of specimen in-plane size on the mechanical behavior of aluminum hexagonal honeycombs. Mat Sci Eng A-Struct 635, 23-35.
[43] Yan C, Hao L, Hussein A, Raymont D (2012). Evaluations of cellular lattice structures manufactured using selective laser melting. Int J Mach Tool Manu 62, 32-38.
[44] Gümrük R, Mines RA (2013). Compressive behaviour of stainless steel micro-lattice structures. Int J Mech Sci 68, 125-139.

[45] Huissein A, Hao L, Yan C, Everson R, Young P (2013). Advanced lattice support structures for metal additive manufacturing. J Mater Process Tech 213, 1019-1026.
[46] Ahmadi SM, Campoli G, Amin Yavari S, Sajadi B, Wauthle R, Schrooten J, Weinans H, Zadpoor AA (2014). Mechanical behavior of regular open-cell porous biomaterials made of diamond lattice unit cells. J Mech Behav Biomed 34, 106-115.
[47] Maskery I, Aremu AO, Simonelli M, Tuck C, Wildman RD, Ashcroft IA, Hague RJ (2015). Mechanical properties of Ti-6Al-4V selectively laser melted parts with body-centered-cubic lattices of varying cell size. Exp Mech 55, 1261-1272.
[48] Maskery I, Aboulkhair NT, Aremu AO, Tuck CJ, Ashcroft IA (2017). Compressive failure modes and energy absorption in additively manufactured double gyroid lattices. Additive Manufacturing 16, 24-29.
[49] Leary M, Mazur M, Elambasseril J, McMillan M, Chirent T, Sun Y, Qian M, Easton M, Brandt M (2016). Selective laser melting (SLM) of AlSi12Mg lattice structures. Mater Design 98, 344-357.
[50] De Pasquale G, Montemurro M, Catapano A, Bertolino G, Revelli L (2017). Cellular structures from additive processes: design, homogenization and experimental validation. Procedia Struct Int, in press.
[51] De Pasquale G, Bertolino G, Luceri F (2017). Design methods for AM lightweight structures: analytic modeling and validation. Proc. AIV, Firenze, Italy.
[52] Leuders S, Thöne M, Riemer A, Niendorf T, Tröster T, Richard HA, Maier HJ (2013). On the mechanical behavior of titanium alloy TiAl6V4 manufactured by selective laser melting: fatigue resistance and crack growth performance. Int J Fatigue 48, 300-307.
[53] Dong L, Deshpande V, Wadley H (2015). Mechanical response of Ti-6Al-4V octet-truss lattice structures. Int J Solids Struct 60-61, 107-124.
[54] De Pasquale G, Montemurro M, Catapano A, Bertolino G, Revelli L (2017). Cellular structures from additive processes: design, homogenization and experimental validation. Sub. To Procedia Engineer.
[55] Catapano A, Montemurro M (2014). A multi-scale approach for the optimum design of sandwich plates with honeycomb core. Part I: homogenisation of core properties. Compos Struct 118, 664-676.
[56] Catapano A, Montemurro M (2014). A multi-scale approach for the optimum design of sandwich plates with honeycomb core. Part II: the optimization strategy. Compos Struct 118, 677-690.

[XXX] Mohammad A, Alahmari AM, Mohammed MK, Renganayagalu RK, Moiduddin K (2017). Effect of energy input on microstructure and mechanical properties of titanium aluminide alloy fabricated by the additive manufacturing process of electron beam melting. Materials 10, 211.